A beam model for the fracture of adhesive joints with dissimilar metal adherends

A.B. de Morais

PII: S0143-7496(22)00029-X

DOI: https://doi.org/10.1016/j.ijadhadh.2022.103112

Reference: JAAD 103112

To appear in: *International Journal of Adhesion and Adhesives*

Received Date: 3 January 2022

Accepted Date: 14 January 2022

Please cite this article as: de Morais AB, A beam model for the fracture of adhesive joints with dissimilar metal adherends, https://doi.org/10.1016/j.ijadhadh.2022.103112.

A beam model for the fracture of adhesive joints with dissimilar metal adherends

A. B. de Morais[1,2]

[1]Department of Mechanical Engineering, University of Aveiro, Campus Santiago, 3810-193 Aveiro, Portugal.

(Tel.: +351 234 370830; E-mail: abm@ua.pt)

[2]Research Centre for Risks and Sustainability in Construction (RISCO), Department of Civil Engineering, University of Aveiro, Campus Santiago, 3810-193 Aveiro, Portugal

Abstract

The natural ability to join different materials is one of the main advantages of adhesive joints. It is thus important to characterize the fracture resistance of adhesive joints with dissimilar materials, as they are increasingly used in relevant industrial applications. There are, however, well-known problems in data analysis of such tests, especially where mode partitioning is concerned. A beam model is here developed for mixed-mode I-II fracture testing on adhesive joints with dissimilar metal adherends. The model predicts quite accurately the strain-energy release rate, the mode-mix and the load-point displacements with fully closed-form equations. Therefore, it can be the basis of future data reduction schemes for fracture tests. Furthermore, it is shown that a wide range of mode-mix combinations can be achieved with simple well-known tests on dissimilar metal adherend joints. They could thus be an interesting alternative to developed mixed-mode I-II tests that require complex test fixtures.

Keywords: B. Metals; C. Fracture mechanics; C. Fracture; Beam model

1. Introduction

The increasing concerns about resource sustainability and greenhouse gas emissions are a major driving force for improved product designs. This often demands combining dissimilar

materials in order to benefit from advantageous characteristics of each material. One of the most striking examples of the search for energy efficiency can be found in the automotive industry, where car bodies combine several aluminium alloys with mild and high strength steels [1]. Adhesive bonding offers several advantages in joining dissimilar substrates e.g. high strength, sealing and improved corrosion resistance. Its limitations can be currently compensated for by employing hybrid joints e.g. adhesive bonding combined with spot-welding [1]. Nonetheless, the current uncertainties in adhesive joint strength prediction still impose conservative design solutions [2], despite the availability of advanced finite element analysis (FEA) codes with cohesive zone modelling (CZM). Such models require preliminary measurement of fracture properties in coupon tests, which nowadays cover the full range mixed-mode I-II loadings using bonded specimens with identical adherends [3]. Furthermore, crack propagation is expected to take place within the bondline for adequately prepared adherend surfaces. In these circumstances, fracture properties measured for a specific adhesive should also apply for joints with dissimilar adherends. Nevertheless, there are good reasons for conducting fracture tests on such joints i.e.:

- increased sensitivity to hygrothermal conditions brought about by the different adherend thermal expansion coefficients;
- possibility of achieving mode-mix combinations with simple specimens, thereby avoiding elaborate fixtures developed for specimens with identical adherends [4-6]

On the other hand, well-known beam theory based data analysis schemes are available for specimens with identical adherends. Specimens with dissimilar adherends are in turn much more difficult to analyse. In fact, the analysis has often been conducted within the framework of the “bi-material” interface issue, which has been the subject of a vast number of studies recently reviewed in [7]. Nonetheless, a comprehensive beam modelling approach was developed by Bennati et al. [8,9] for the asymmetric double cantilever beam specimen

(ADCB) applied to delamination of composites. Moreover, it was recently shown in [10] that such beam theory framework was appropriate for other specimens covering the entire range of mixed-mode I-II loadings. In addition, the complexity of the analysis could be considerably reduced after considering the physical meaning of the solutions together with the typical material properties and specimen geometries [10]. However, the beam models presented in [8-10] concern delamination of composites and thus do not consider an adhesive layer. Instead, tractions are related to separations via cohesive stiffnesses that depend on laminate through-thickness moduli and characteristic thicknesses calibrated by FEA [8-10]. The scenario is different in metal adhesive joints, as the high adherend stiffness means that tractions are dictated by bondline deformations. In fact, it has been shown that even common thin bondlines influence the specimen compliance and strain-energy release rates of the well-known double cantilever beam (DCB) [11] and end-notched flexure (ENF) specimens [12]. Evidently, such influence increases when more flexible adhesives and/or thicker bondlines are employed.

Several beam models have already been presented for adhesive joints with dissimilar adherends, including the more general Timoshenko beam theory e.g. [13-14] and composite adherends [13]. Such models have been applied to lap-joints with adherends under tensile loads, providing quite accurate bondline shear and peel stress distributions [13,14]. It is also worth mentioning that Alfredsson and Högberg [15] used an Euler-Bernoulli beam model to analyse the End-Loaded Split (ELS) specimen with dissimilar adherends. They [15] developed solutions for the *J*-integral and showed the large effect of the bondline on specimen compliance and strain-energy release rate.

The beam model here developed considers explicitly thin (h_a = 0.2 mm) to moderately thick (h_a = 1 mm) bondlines. Solutions are presented for metal adherends, focussing on several combinations of steel and aluminium adherends with different thicknesses h_1 and h_2.

The specimen selected is here named force-loaded double cantilever beam (FLDCB) (Fig. 1). It has an a-long crack and a built-in support at the end of the span L. This specimen was actually implemented in [5] using a dual-actuator to apply the transverse loads F_1 and F_2, thereby requiring specific testing equipment seldom used. As shown below, the present dissimilar adherends beam model (DABM) gives quite accurate predictions of the strain-energy release rate, mode-mix and load-point displacements for a wide range of mixed-mode I-II loadings.

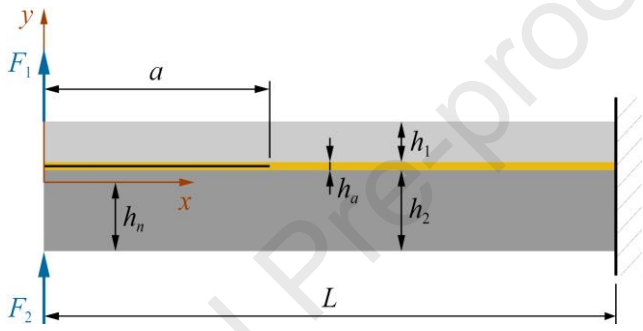

Fig. 1. The force-loaded double cantilever beam specimen (FLDCB).

Finally, this work confirms the great potential of dissimilar metal adhesively bonded specimens for attaining a wide range of mode-mix combinations with well-known simple tests. This reinforces the usefulness of the analytical framework provided by the DABM.

2. The dissimilar metal adherends beam model (DABM)

2.1. Fundamental equations and assumptions

Each adherend is here modelled as a Timoshenko beam. The analysis begins with the equilibrium equations of infinitesimal elements of the upper (1) and lower (2) adherends in the bonded $a \leq x \leq L$ region of the FLDCB specimen (Figs. 1 and 2). The element cross-sections are subjected to normal forces N, which must be symmetric for horizontal force equilibrium, transverse shear forces V_i and bending moments M_i (i = 1, 2). As a result of

adhesive deformations, the normal σ_c and shear τ_c tractions act on the adherend bonded surfaces. It is worth noting that the sign convention here adopted takes as positive the forces, moments and tractions depicted in Fig. 2. Letting b designate the specimen width, the horizontal force equilibrium equation is

$$\frac{dN}{dx} = b\tau_c \tag{1}$$

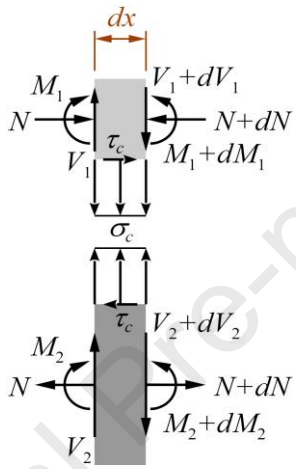

Fig. 2. Forces, moments and tractions acting on infinitesimal elements of the upper (1) and lower (2) adherends of the FLDCB specimen $a \leq x \leq L$ region (Fig. 1).

The remaining equilibrium equations are somewhat sensitive to the assumption that tractions are constant across the bondline thickness. This assumption proved to be an adequate approximation for bondlines up to h_a = 3 mm of ENF specimens with identical metal adherends [16]. Since the FLDCB specimens here analysed also involve thicker and much stiffer metal adherends than the bondline, this assumption was deemed appropriate for this study. In these circumstances, vertical force equilibrium of a part of the specimen from the free ends (x = 0) to an $a \leq x \leq L$ cross-section imposes that

$$V_1 + V_2 + bh_a\tau_c = F_1 + F_2 \tag{2}$$

The vertical force equilibrium equations of the adherend elements (Fig. 2) are thus

$$\frac{dV_1}{dx} = -b\sigma_c - \frac{bh_a}{2}\frac{d\tau_c}{dx} \tag{3}$$

$$\frac{dV_2}{dx} = b\sigma_c - \frac{bh_a}{2}\frac{d\tau_c}{dx} \tag{4}$$

since part of the F_1 and F_2 applied forces are absorbed by the bondline. Moment equilibrium for the i-th adherend is expressed as

$$V_i = \frac{dM_i}{dx} + \frac{bh_i\tau_c}{2} \tag{5}$$

Eqs. (3)-(5) can be combined in order to obtain

$$\frac{d^2M_1}{dx^2} = -b\sigma_c - \frac{b(h_1+h_a)}{2}\frac{d\tau_c}{dx} \tag{6}$$

$$\frac{d^2M_2}{dx^2} = b\sigma_c - \frac{b(h_2+h_a)}{2}\frac{d\tau_c}{dx} \tag{7}$$

which are convenient for subsequent derivations.

The adherend behaviour is, to a very large extent, dictated by the beam theory (BT) fundamental relation

$$M_i = E_i I_i \frac{d^2v_{b,i}}{dx^2} \tag{8}$$

where E_i is the i-th adherend Young's modulus, $I_i = bh_i^3/12$ the second moment of area and $v_{b,i}$ the vertical bending displacement. Nevertheless, transverse shear is also taken into account in the scope of Timoshenko BT. Transverse shear displacements $v_{s,i}$ are thus given by

$$\frac{dv_{s,i}}{dx} = -\frac{V_i}{f_s bh_i G_i} \tag{9}$$

where G_i is the i-th adherend shear modulus and $f_s = 5/6$ is the transverse shear factor for rectangular cross-sections. At this stage, it is worth remarking that Eq. (9) bears a simplification identified in [10] for delamination of composites: it was developed from energy methods for the parabolic through-thickness transverse shear stress (τ_s) distribution that exists in beams. Such distribution is characterized by a maximum $\tau_s = 3V_i/2bh_i$ at the mid-plane and $\tau_s = 0$ at the surfaces. This distribution is appropriate for the pre-cracked region, given the small contribution of the bondline for the load-displacement response. However, it does not

hold for the bonded $a \leq x \leq L$ region under analysis, since τ_c acts on the bonded surface. Nonetheless, as discussed in [10], adopting a more accurate formulation would lead to non-linear differential equations whose complexity compromises the practical usefulness of beam modelling altogether. Moreover, as demonstrated below, the load-displacement and, consequently, the strain-energy release rate and mode partitioning are clearly dominated by the bending moments. Therefore, Eq. (9) is retained with $f_s = 5/6$.

As for the tractions, linear elasticity is assumed for the bondline, as the main goal of this work is to provide the basic framework for fracture testing of dissimilar metal adhesively bonded specimens. It is also assumed that, owing to the high adherend stiffness, tractions are dictated by bondline deformations. As mentioned above, this contrasts with delamination of composites, where the elastic traction-separation law involves cohesive stiffnesses that depend on laminate through-thickness moduli and on characteristic thicknesses calibrated by FEA [10]. Previous work on mode I fracture showed the adequacy of the in-plane restrained hypothesis for the bondline [11] i.e. owing to the much higher stiffness of the metal adherends, $\varepsilon_x \approx 0$ and $\varepsilon_y \approx 0$ prevail in the bondline. This allows the normal traction to be expressed as

$$\sigma_c = \frac{E_{as}}{h_a}\delta_n \tag{10}$$

where the uni-axial strain adhesive modulus is obtained from the adhesive Young's modulus E_a and Poisson's ratio ν_a as

$$E_{as} = \frac{E_a(1-\nu_a)}{1-\nu_a-2\nu_a^2} \tag{11}$$

and

$$\delta_n = v_1 - v_2 \tag{12}$$

is the normal separation, expressed as function of the vertical beam displacements

$$v_i = v_{b,i} + v_{s,i} \tag{13}$$

of each adherend. The shear traction is, evidently,

$$\tau_c = \frac{G_a}{h_a}\delta_s \tag{14}$$

where G_a is the adhesive shear modulus and δ_s the shear separation. As seen in [10,16], δ_s depends on the bending cross-section rotations of each adherend, which are $dv_{b,i}/dx$ in the geometrically linear regime, and on the uniform cross-section displacements caused by N (Fig. 2). Adopting the $\delta_s \geq 0$, $N \geq 0$ and $dv_{b,i}/dx \leq 0$ sign conventions,

$$\begin{aligned}\delta_s(x) - \delta_s(L) = {} & \frac{h_1+h_a}{2}\left[\left.\frac{dv_{b,1}}{dx}\right|_L - \left.\frac{dv_{b,1}}{dx}\right|_x\right] \\ & + \frac{h_2+h_a}{2}\left[\left.\frac{dv_{b,2}}{dx}\right|_L - \left.\frac{dv_{b,2}}{dx}\right|_x\right] \\ & - \left(\frac{1}{E_1 h_1} + \frac{1}{E_2 h_2}\right)\int_x^L \frac{N}{b}\,dx\end{aligned} \tag{15}$$

It is worth remarking that Eq. (15) differs from the analogous relation adopted in most beam models e.g. [12-15] that consider thin bondlines by introducing terms on h_a. Such terms result from the rotation effect on adhesive shear strains and allowed the accurate modelling of metal adhesively bonded ENF specimens with thick bondelines i.e. up to h_a = 3.0 mm [16]. Although such thick bondlines are not analysed in this work, similar to [16], adopting Eq. (15) was expected to result in improved accuracy relative to the common thin bondline hypothesis.

Therefore, one should bear in mind that the DABM assumes:

- the hypotheses inherent to Timoshenko BT, including the approximate treatment of transverse shear seen above;
- that tractions are dictated by bondline deformations, given the high adherend stiffness;
- uniform tractions across the bondline thickness, an approximation that finds support in the larger adherend thickness and much higher adherend moduli;
- adherend linear elastic behaviour, a condition expected to hold for fracture specimens;
- adhesive linear elastic behaviour, which only applies during the initial loading stages;

- in-plane restrained adhesive for the normal traction-separation law, owing to the high thickness and moduli of the fracture specimen adherends.

The penultimate assumption seems clearly the most limiting for practical application of the DABM. At this stage, however, there good reasons to adopt such assumption i.e.:

- The current state-of-the-art in fracture of dissimilar adherend joints, especially where mode partitioning is concerned [7];
- DABM extension to include adhesive plasticity and damage can be envisaged by adopting appropriate mixed-mode traction-separation laws. Nonetheless, this will bring about more complex equations and solution procedures;
- It may be possible to apply the DABM with the effective crack concept [3,11,12,16], which takes into account the so-called fracture process zone (FPZ), where adhesive plasticity and damage take place. This would mean replacing the crack length a by a larger effective crack length to be determined from experimental specimen compliance data. However, this approach needs to be assessed in future work.

2.2. Solutions for the tractions

Solutions for $\tau_c(x)$ and $\sigma_c(x)$ can be obtained without having to introduce any condition specific of the FLDCB specimen (Fig. 1). In fact, although Eq. (2) was invoked to derive Eqs. (3) and (4), the latter apply to any region which is under no additional external load. We begin by substituting $h_a\tau_c/G_a$ of Eq. (14) for δ_s in Eq. (15) and performing three consecutive differentiations. On the resulting equation, the term involving N can be expressed as a function of $d\tau_c/dx$ using Eq. (1), while the terms on $d^4v_{b,i}/dx^4$ can be written as functions of $d\tau_c/dx$ and σ_c using Eqs. (6)-(8). This provides a useful relation between the tractions

$$\sigma_c = R_3 \frac{d^3\tau_c}{dx^3} + R_1 \frac{d\tau_c}{dx} \tag{16}$$

with the material properties and geometry dependent traction factors

$$R_1 = \frac{\frac{h_1^2+3(h_1+h_a)^2}{6E_1h_1^3}+\frac{h_2^2+3(h_2+h_a)^2}{6E_2h_2^3}}{\frac{h_2+h_a}{E_2h_2^3}-\frac{h_1+h_a}{E_1h_1^3}} \tag{17}$$

$$R_3 = \frac{h_a}{6G_a\left(\frac{h_1+h_a}{E_1h_1^3}-\frac{h_2+h_a}{E_2h_2^3}\right)} \tag{18}$$

Substitution of Eq. (16) for σ_c in Eqs. (6) and (7) gives

$$\frac{d^2M_i}{dx^2} = Q_{i,3}\frac{d^3\tau_c}{dx^3} + Q_{i,1}\frac{d\tau_c}{dx} \tag{19}$$

where the material properties and geometry dependent parameters are

$$Q_{1,3} = -Q_{2,3} = -R_3 \tag{20}$$

$$Q_{1,1} = -b\left(R_1 + \frac{h_1+h_a}{2}\right), Q_{2,1} = b\left(R_1 - \frac{h_2+h_a}{2}\right) \tag{21}$$

Yet, σ_c is also given by Eq. (10), in which Eqs. (12) and (13) can be used first for expressing δ_n as a function of $v_{b,i}$ and $v_{s,i}$. Successive differentiation combined with Eqs. (5), (8) and (9) leads to

$$\begin{aligned}\frac{h_a}{E_{as}}\frac{d^4\sigma_c}{dx^4} &= \frac{1}{E_1I_1}\frac{d^2M_1}{dx^2} - \frac{1}{E_2I_2}\frac{d^2M_2}{dx^2} \\ &+ \frac{6}{5bh_2G_2}\left(\frac{d^4M_2}{dx^4} + \frac{bh_2}{2}\frac{d^3\tau_c}{dx^3}\right) \\ &- \frac{6}{5bh_1G_1}\left(\frac{d^4M_1}{dx^4} + \frac{bh_1}{2}\frac{d^3\tau_c}{dx^3}\right)\end{aligned} \tag{22}$$

One can now substitute Eq. (16) for σ_c and Eqs. (19) for the M_i-derivatives in order to arrive at the 7th-order linear homogeneous differential equation

$$\frac{h_a}{G_a}\frac{d^7\tau_c}{dx^7} + D_5\frac{d^5\tau_c}{dx^5} + D_3\frac{d^3\tau_c}{dx^3} + D_1\frac{d\tau_c}{dx} = 0 \tag{23}$$

with coefficients

$$\begin{aligned}D_1 = -\frac{12E_{as}}{h_a}&\left(\frac{1}{E_1h_1}+\frac{1}{E_2h_2}\right)\left(\frac{1}{E_1h_1^3}+\frac{1}{E_2h_2^3}\right) \\ &+\frac{3(h_1+h_2+2h_a)^2}{E_1E_2(h_1h_2)^3}\end{aligned} \tag{24}$$

$$D_3 = \frac{6E_{as}}{5h_a}\left(\frac{1}{G_1h_1}+\frac{1}{G_2h_2}\right)\left(\frac{4h_1+3h_a}{E_1h_1^2}+\frac{4h_2+3h_a}{E_2h_2^2}\right) + \frac{12E_{as}}{E_1h_1^3}\left(\frac{3(h_1+h_a)}{5G_2h_2}+\frac{1}{G_a}\right) + \frac{12E_{as}}{E_2h_2^3}\left(\frac{3(h_2+h_a)}{5G_1h_1}+\frac{1}{G_a}\right) \quad (25)$$

$$D_5 = -\frac{h_1^2+3(h_1+h_a)^2}{E_1h_1^3} - \frac{h_2^2+3(h_2+h_a)^2}{E_2h_2^3} - \frac{6E_{as}}{5G_a}\left(\frac{1}{G_1h_1}+\frac{1}{G_2h_2}\right) \quad (26)$$

The solution of Eq. (23) is established by finding the 7 roots of the characteristic polynomial on s

$$s\left(\frac{h_a}{G_a}s^6 + D_5s^4 + D_3s^2 + D_1\right) = 0 \quad (27)$$

one of which is, evidently, $s = 0$. The remaining solutions are easily found by converting the 6th-order polynomial of Eq. (27) into a 3rd-order polynomial on s^2. For the combinations of metal adherend, adhesive properties and thicknesses here considered, the 6th-order polynomial of Eq. (27) has one pair of real roots and two pairs of complex conjugate roots. Therefore, the solution of Eq. (23) can be written as

$$\tau_c = \tau_0 + \tau_1 e^{-\lambda x} + e^{-\mu x}(\tau_2 \cos \omega x + \tau_3 \sin \omega x) + \tau_4 e^{\lambda x} + e^{\mu x}(\tau_5 \cos \omega x + \tau_6 \sin \omega x) \quad (28)$$

where τ_k are integration constants, λ and μ are elastic exponential traction distribution parameters and ω is an elastic sinusoidal traction distribution parameter. The Appendix presents closed-form solutions for λ, μ and ω. Finally, substitution of Eq. (28) for τ_c in Eq. (16) provides

$$\sigma_c = \sigma_1 e^{-\lambda x} + e^{-\mu x}(\sigma_2 \cos \omega x + \sigma_3 \sin \omega x) + \sigma_4 e^{\lambda x} + e^{\mu x}(\sigma_5 \cos \omega x + \sigma_6 \sin \omega x) \quad (29)$$

with σ_k being integration constants related to τ_k.

It can be shown that the DABM becomes equal to the beam models of [11,16] for mode I and mode II fracture of adhesive joints with identical metal adherends. It is worth reminding that this simpler case involves decoupled 3rd-order and 4th-order linear differential equations

for τ_c and σ_c, respectively, The solution for τ_c is free from sinusoidal terms, while the one for σ_c only retains sinusoidal terms.

2.3. Physical meaning and simplification of the solutions

The above solutions for the tractions are expected to apply along the entire bonded $a \leq x \leq L$ region of FLDCB specimens (Fig. 1). Although beam modelling suppresses the crack-tip singularity, it is evident that σ_c and τ_c attain peak values at the $x = a$ crack-tip position, and then decrease gradually. If the $x = L$ built-in cross-section (Fig. 1) is distant enough from the crack-tip, the terms on $e^{\lambda x}$ and $e^{\mu x}$ should be negligible there i.e.

$$\tau_c \approx \tau_0 + \tau_1 e^{-\lambda x} + e^{-\mu x}(\tau_2 \cos \omega x + \tau_3 \sin \omega x) \tag{30}$$

$$\sigma_c \approx \sigma_1 e^{-\lambda x} + e^{-\mu x}(\sigma_2 \cos \omega x + \sigma_3 \sin \omega x) \tag{31}$$

in the vicinity of the $x = a$ crack-tip position.

Secondly, in a mid-region sufficiently away from both the crack-tip and built-in cross-sections, the tractions should model the response of an uncracked beam. Accordingly, $\sigma_c = 0$ and $\tau_c = \tau_0$ must be compatible with the through-thickness transverse shear stress distribution $\tau_s(y)$. In order to verify such compatibility, a common mechanics of materials analysis of bending and transverse shear of the uncracked bonded region was conducted. The through-thickness distribution of σ_x normal stresses resulting from bending is assumed to be linear. This enables the determination of:

- the neutral surface vertical position h_n (Fig. 1) relative to the specimen lower surface;
- the uncracked beam bending stiffness.

The horizontal force equilibrium of an uncracked beam element with infinitesimal length dx and delimited by:

- the upper specimen surface;
- an internal surface of y-coordinate not inside the bondline (Fig. 1);

shows that $\tau_s(y)$ is parabolic. In particular, at the adherend bonded surfaces, τ_s is equal to

$$\tau_0 = \frac{3(F_1+F_2)E_1h_1[h_1+2(y_2+h_a)]}{2b\{E_2(y_2^3+h_n^3)+E_1[(y_2+h_a+h_1)^3-(y_2+h_a)^3]\}} \quad (32)$$

where

$$h_n = \frac{E_2h_2^2+E_1h_1[2(h_2+h_a)+h_1]}{2(E_2h_2+E_1h_1)} \quad (33)$$

$$y_2 = h_2 - h_n \quad (34)$$

is the vertical coordinate of the lower adherend bonded surface (Fig. 1). It is worth mentioning that this analysis neglects the contribution of adhesive axial stresses to the uncracked beam bending stiffness, hence the absence of terms on E_a in Eqs. (32) and (33). This is clearly a realistic assumption for metal adherends, since $E_a << E_1, E_2$.

Finally, near the $x = L$ built-in cross-section, the terms of Eqs. (28) and (29) on $e^{-\lambda x}$ and $e^{-\mu x}$ should be negligible and the tractions must comply with the clamp conditions. In particular, for the ideal built-in end here assumed, $\sigma_c(L) = 0$ and $\tau_c(L) = 0$. In the scope of beam modelling, it seems reasonable to neglect σ_c altogether in the vicinity of $x = L$. However, τ_c must decrease from τ_0 to 0, and thus we consider

$$\tau_c \approx \tau_0 + \tau_4 e^{\lambda x} \quad (35)$$

close to $x = L$ (Fig. 1). This is similar to the τ_c decrease from the crack-tip to the load-point of the ENF specimen [12,16]. Moreover, the ideal built-in end condition $\tau_c(L) = 0$ provides directly

$$\tau_4 \approx -\tau_0 e^{-\lambda L} \quad (36)$$

Besides reducing the number of integration constants to be determined, this simplified approach has other important advantages:

- it enables strain-energy release rate and mode partitioning determination from crack-tip section forces and moments;
- it greatly reduces the overall complexity of the problem at hands and the number of

calculations to be made;

- it applies to sufficiently large ($L - a$) distances (Fig. 1) which should be adopted in actual tests in order to accommodate the long FPZ developed by tough adhesives, especially under high mode II loadings.

In fact, previous work [12,16] on ENF specimens bonded with identical metal adherends showed that artificially high perceived toughness values may be measured if the FPZ gets too close to the load-point position. First of all, the analyses of such situations demand extension of the DABM to include bondeline plasticity and softening. Furthermore, the full traction solutions expressed by Eqs. (28) and (29) are needed, thereby complicating considerably calculations, hence also experimental data reduction. Therefore, this work is restricted to the large ($L - a$) case.

Naturally, the question that arises here is how large should ($L - a$) be for ensuring the accuracy of Eqs. (30), (31), (35) and (36). As in common fracture specimens bonded with identical adherends [11,12,16], the decrease of τ_c from $\tau_c(a)$ to τ_0:

- takes place along a much larger distance than the one of $\tau_c \approx \tau_0$ to $\tau_c = 0$ near $x = L$;
- ends-up being dictated by the term on $e^{-\lambda x}$ of Eq. (30).

Accordingly, one criterion to define the minimum ($L - a$) can be based on $\{\tau_0 + \tau_1 e^{-\lambda L}\}$ being a small tolerance above τ_0 e.g. 0.1 %. This criterion is adopted below in Section 3. Nevertheless, given the exponential nature of the functions involved and the errors in model predictions one may wish to tolerate, other criteria can be used to define minimum ($L - a$) distances.

2.4. Strain-energy release rate components

In the framework outlined above, one should substitute Eq. (30) for τ_c in Eq. (19) and perform a first integration that, combined with Eq. (5), provides the adherend transverse forces

$$V_i = C_{i,3} + \left(Q_{i,1} + \frac{bh_i}{2}\right)\tau_0 + \tau_1 e^{-\lambda x}\left(Q_{i,3}\lambda^2 + Q_{i,1} + \frac{bh_i}{2}\right)$$
$$+\tau_2 e^{-\mu x}\left[\left(Q_{i,3}(\mu^2-\omega^2) + Q_{i,1} + \frac{bh_i}{2}\right)\cos\omega x + Q_{i,3}(2\mu\omega)\sin\omega x\right] \quad (37)$$
$$+\tau_3 e^{-\mu x}\left[\left(Q_{i,3}(\mu^2-\omega^2) + Q_{i,1} + \frac{bh_i}{2}\right)\sin\omega x - Q_{i,3}(2\mu\omega)\cos\omega x\right]$$

while a second integration gives the adherend bending moments

$$M_i = C_{i,2} + \left(Q_{i,1} + C_{i,3}\right)\tau_0 x - \tau_1 e^{-\lambda x}\left(Q_{i,3}\lambda + \frac{Q_{i,1}}{\lambda}\right)$$
$$-\tau_2 e^{-\mu x}\left[\left(Q_{i.3} + \frac{Q_{i,1}}{\mu^2+\omega^2}\right)\mu\cos\omega x + \left(Q_{i.3} - \frac{Q_{i,1}}{\mu^2+\omega^2}\right)\omega\sin\omega x\right] \quad (38)$$
$$-\tau_3 e^{-\mu x}\left[\left(Q_{i.3} + \frac{Q_{i,1}}{\mu^2+\omega^2}\right)\mu\sin\omega x - \left(Q_{i.3} - \frac{Q_{i,1}}{\mu^2+\omega^2}\right)\omega\cos\omega x\right]$$

in the vicinity of the crack-tip, $C_{i,3}$ and $C_{i,2}$ being integration constants. The latter can be determined as functions of τ_k (k = 0-3) by imposing that Eqs. (30), (31), (37) and (38) comply with:

- the kinematics of shear deformation Eq. (15), whose double differentiation combined with Eqs. (8) and (14) gives

$$\frac{h_a}{G_a}\frac{d^2\tau_c}{dx^2} + \frac{h_1+h_a}{2E_1I_1}\frac{dM_1}{dx} + \frac{h_2+h_a}{2E_2I_2}\frac{dM_2}{dx} - \left(\frac{1}{E_1h_1} + \frac{1}{E_2h_2}\right)\tau_c = 0 \quad (39)$$

- the normal traction as obtained from Eqs. (3) and (4),

$$\sigma_c = \frac{1}{2b}\left(\frac{dV_2}{dx} - \frac{dV_1}{dx}\right) \quad (40)$$

This results in

$$C_{1,3} = \frac{E_1h_1^3(h_2+h_a)}{h_1+h_2+2h_a}\left(\frac{Q_{2,1}}{E_2h_2^3} - \frac{Q_{1,1}}{E_1h_1^3}\right)\tau_0 \quad (41)$$

$$C_{2,3} = -\frac{E_2h_2^3(h_1+h_a)}{h_1+h_2+2h_a}\left(\frac{Q_{2,1}}{E_2h_2^3} - \frac{Q_{1,1}}{E_1h_1^3}\right)\tau_0 \quad (42)$$

$$C_{1,2} = \frac{E_1bh_1^3}{6(h_1+h_2+2h_a)}\left(\frac{1}{E_1h_1} + \frac{1}{E_2h_2}\right)C_N \quad (43)$$

$$C_{2,2} = \frac{E_2bh_2^3}{6(h_1+h_2+2h_a)}\left(\frac{1}{E_1h_1} + \frac{1}{E_2h_2}\right)C_N \quad (44)$$

where

$$C_N = \tau_0 a - \frac{\tau_1}{\lambda} e^{-\lambda a} - \frac{\tau_2 e^{-\mu a}}{\mu^2+\omega^2}(\mu \cos \omega a - \omega \sin \omega a) - \frac{\tau_3 e^{-\mu a}}{\mu^2+\omega^2}(\mu \sin \omega a + \omega \cos \omega a) \quad (45)$$

At this stage, it is interesting to invoke the condition regarding adherend crack-tip section transverse shear forces (Fig. 1),

$$V_1(a) + V_2(a) = F_1 + F_2 \quad (46)$$

In fact, using Eq. (37) to compute $V_i(a)$ one obtains τ_0 identical to Eq. (32), thereby confirming that the DABM is compatible with the through-thickness τ_s distribution of the uncracked beam. The remaining τ_1, τ_2 and τ_3 integration constants can be determined from

$$V_1(a) = F_1 \text{ or } V_2(a) = F_2 \quad (47)$$

$$M_1(a) = F_1 a, M_2(a) = F_2 a \quad (48)$$

using Eq. (38) to calculate $M_i(a)$. The normal traction integration constants of Eq. (31) are then easily calculated from Eqs. (16)-(18) and (30).

$$\sigma_1 = -\tau_1(R_3\lambda_1^3 + R_1\lambda_1) \quad (49)$$

$$\sigma_2 = -\tau_2\mu[R_3(\mu^2 - 3\omega^2) + R_1] + \tau_3\omega[R_3(3\mu^2 - \omega^2) + R_1] \quad (50)$$

$$\sigma_3 = -\tau_2\omega[R_3(3\mu^2 - \omega^2) + R_1] - \tau_3\mu[R_3(\mu^2 - 3\omega^2) + R_1] \quad (51)$$

Finally, one can compute successively:

- the crack-tip tractions $\tau_c(a)$ and $\sigma_c(a)$ from Eqs. (30) and (31), respectively;
- the $\delta_n(a)$ and $\delta_s(a)$ separations from Eqs. (10) and (14), respectively;
- the mode I and mode II strain-energy release rates; since gradual damage in a cohesive zone is not considered here, the sharp tractions decrease to null values of virtual infinitesimal propagation means that $G_I = \sigma_c(a)\delta_n(a)/2$ and $G_{II} = \tau_c(a)\delta_s(a)/2$, which Eqs. (10) and (14) allow be expressed as:

$$G_I = \frac{h_a\sigma_c^2(a)}{2E_{as}}, G_{II} = \frac{h_a\tau_c^2(a)}{2G_a} \quad (52)$$

It is worth remarking that the solutions obtained in this section for G_I and G_{II}:

- Only require fully closed-form calculations i.e. no numerical procedures are needed. Nevertheless, no attempt was made to develop shortened expressions, as the entire process is easily handled in common spreadsheet software;
- Although the FLDCB specimen (Fig. 1) was adopted as reference for the present analysis, Eqs. (30), (31) and (52) apply to any other fracture specimen whose loads and supports are sufficiently distant from the crack-tip. It is only a matter of using the appropriate crack-tip transverse shear and bending moments to determine the τ_k (k = 0-3) and σ_k (k = 1-3) integration constants.

2.5. Load-displacement responses

In order to derive the load-displacement response of the FLDCB specimen (Fig. 1), it is convenient to combine Eqs. (30), (35) and (36) into a more general solution

$$\tau_c = \tau_0 + \tau_1 e^{-\lambda x} + e^{-\mu x}(\tau_2 \cos \omega x + \tau_3 \sin \omega x) - \tau_0 e^{\lambda(x-L)} \tag{53}$$

This implies adding the exponential term that becomes relevant near the clamp to Eqs. (37) and (38), which become

$$\begin{aligned} V_i = {} & C_{i,3} + \left(Q_{i,1} + \frac{bh_i}{2}\right)\tau_0 + \left(\tau_1 e^{-\lambda x} - \tau_0 e^{\lambda(x-L)}\right)\left(Q_{i,3}\lambda^2 + Q_{i,1} + \frac{bh_i}{2}\right) \\ & + \tau_2 e^{-\mu x}\left[\left(Q_{i,3}(\mu^2 - \omega^2) + Q_{i,1} + \frac{bh_i}{2}\right)\cos \omega x + Q_{i,3}(2\mu\omega)\sin \omega x\right] \\ & + \tau_3 e^{-\mu x}\left[\left(Q_{i,3}(\mu^2 - \omega^2) + Q_{i,1} + \frac{bh_i}{2}\right)\sin \omega x - Q_{i,3}(2\mu\omega)\cos \omega x\right] \end{aligned} \tag{54}$$

$$\begin{aligned} M_i = {} & C_{i,2} + (Q_{i,1} + C_{i,3})\tau_0 x - \left(\tau_1 e^{-\lambda x} + \tau_0 e^{\lambda(x-L)}\right)\left(Q_{i,3}\lambda + \frac{Q_{i,1}}{\lambda}\right) \\ & - \tau_2 e^{-\mu x}\left[\left(Q_{i.3} + \frac{Q_{i,1}}{\mu^2+\omega^2}\right)\mu \cos \omega x + \left(Q_{i.3} - \frac{Q_{i,1}}{\mu^2+\omega^2}\right)\omega \sin \omega x\right] \\ & - \tau_3 e^{-\mu x}\left[\left(Q_{i.3} + \frac{Q_{i,1}}{\mu^2+\omega^2}\right)\mu \sin \omega x - \left(Q_{i.3} - \frac{Q_{i,1}}{\mu^2+\omega^2}\right)\omega \cos \omega x\right] \end{aligned} \tag{55}$$

The substitution of Eq. (55) for M_i in Eq. (8) yields upon successive integration

$$\begin{aligned} E_i I_i \frac{dv_{b,i}}{dx} &= \left(\tau_1 e^{-\lambda x} - \tau_0 e^{\lambda(x-L)}\right)\left(Q_{i,3} + \frac{Q_{i,1}}{\lambda^2}\right) \\ &+\tau_2 e^{-\mu x}\left[\left(Q_{i,3} + Q_{i,1}\frac{\mu^2-\omega^2}{(\mu^2+\omega^2)^2}\right)\cos\omega x - \frac{2Q_{i,1}\mu\omega}{(\mu^2+\omega^2)^2}\sin\omega x\right] \\ &+\tau_3 e^{-\mu x}\left[\left(Q_{i,3} + Q_{i,1}\frac{\mu^2-\omega^2}{(\mu^2+\omega^2)^2}\right)\sin\omega x + \frac{2Q_{i,1}\mu\omega}{(\mu^2+\omega^2)^2}\cos\omega x\right] \\ &+\tau_0\left(Q_{i,3} + Q_{i,1}\frac{x^2}{2}\right) + C_{i,3}\frac{x^2}{2} + C_{i,2}x + C_{i,1} \end{aligned} \tag{56}$$

$$\begin{aligned} E_i I_i v_{b,i} &= -\left(\tau_1 e^{-\lambda x} + \tau_0 e^{\lambda(x-L)}\right)\left(\frac{Q_{i,3}}{\lambda} + \frac{Q_{i,1}}{\lambda^3}\right) \\ &-\frac{\tau_2 e^{-\mu x}}{\mu^2+\omega^2}\left[\left(Q_{i,3} + Q_{i,1}\frac{\mu^2-3\omega^2}{(\mu^2+\omega^2)^2}\right)\mu\cos\omega x - \left(Q_{i,3} + Q_{i,1}\frac{3\mu^2-\omega^2}{(\mu^2+\omega^2)^2}\right)\omega\sin\omega x\right] \\ &-\frac{\tau_3 e^{-\mu x}}{\mu^2+\omega^2}\left[\left(Q_{i,3} + Q_{i,1}\frac{\mu^2-3\omega^2}{(\mu^2+\omega^2)^2}\right)\mu\sin\omega x + \left(Q_{i,3} + Q_{i,1}\frac{3\mu^2-\omega^2}{(\mu^2+\omega^2)^2}\right)\omega\cos\omega x\right] \\ &+\tau_0\left(Q_{i,3}x + Q_{i,1}\frac{x^3}{6}\right) + C_{i,3}\frac{x^3}{6} + C_{i,2}\frac{x^2}{2} + C_{i,1}x + C_{i,0} \end{aligned} \tag{57}$$

giving rise to the $C_{i,1}$ and $C_{i,0}$ additional integration constants. The latter are easily obtained from the ideal clamp boundary conditions (Fig. 1)

$$E_i I_i \frac{dv_{b,i}}{dx}\Big|_{x=L} = 0, v_{b,i}(L) = 0 \tag{58}$$

by recovering the advantages of the specimen being sufficiently long to make terms on $e^{-\lambda L}$ and $e^{-\mu L}$ negligible, and thus

$$C_{i,1} = \tau_0 Q_{i,1}\left(\frac{1}{\lambda^2} - \frac{L^2}{2}\right) - C_{i,3}\frac{L^2}{2} - C_{i,2}L \tag{59}$$

$$C_{i,0} = \tau_0\left[\left(Q_{i,3} + \frac{Q_{i,1}}{\lambda^2}\right)\left(\frac{1}{\lambda} - L\right) + Q_{i,1}\frac{L^3}{3}\right] + C_{i,3}\frac{L^3}{3} + C_{i,2}\frac{L^2}{2} \tag{60}$$

The substitution of Eq. (54) for V_i in Eq. (9) and subsequent integration provides the transverse shear displacements

$$\begin{aligned} \frac{5G_i bh_i}{6} v_{s,i} &= \left(\tau_1 e^{-\lambda x} + \tau_0 e^{\lambda(x-L)}\right)\left[Q_{i,3}\lambda + \left(Q_{i,1} + \frac{bh_i}{2}\right)\frac{1}{\lambda}\right] \\ &+\tau_2 e^{-\mu x}\left[\left(Q_{i,3} + \frac{2Q_{i,1}+bh_i}{2(\mu^2+\omega^2)}\right)\mu\cos\omega x + \left(Q_{i,3} - \frac{2Q_{i,1}+bh_i}{2(\mu^2+\omega^2)}\right)\omega\sin\omega x\right] \\ &+\tau_3 e^{-\mu x}\left[\left(Q_{i,3} + \frac{2Q_{i,1}+bh_i}{2(\mu^2+\omega^2)}\right)\mu\sin\omega x - \left(Q_{i,3} - \frac{2Q_{i,1}+bh_i}{2(\mu^2+\omega^2)}\right)\omega\cos\omega x\right] \\ &-\tau_0 x\left(Q_{i,1} + \frac{bh_i}{2}\right) - C_{i,3}x - C_{i,2} + C_{i,4} \end{aligned} \tag{61}$$

where the ideal clamp condition $v_{s,i}(L) = 0$ with the negligible terms $e^{-\lambda L}$ and $e^{-\mu L}$ enables the determination of the integration constants

$$C_{i,4} = -\tau_0\left[Q_{i,3}\lambda + \left(Q_{i,1} + \frac{bh_1}{2}\right)\left(\frac{1}{\lambda} - L\right)\right] + C_{i,3}L + C_{i,2} \tag{62}$$

In the end, the load-displacement response is obtained by calculating successively:

- the adherend crack-tip cross-section bending rotations $dv_{b,i}/dx|_{x=a}$, bending displacements $v_{b,i}(a)$ and transverse shear displacements $v_{s,i}(a)$ from Eqs. (56), (57) and (61), respectively;
- the adherend load-point bending and transverse shear displacements by adding the contribution of the uncracked region i.e.

$$v_{b,i}(0) = v_{b,i}(a) - a\left.\frac{dv_{b,i}}{dx}\right|_{x=a} + \frac{F_i a^3}{3E_i I_i} \tag{63}$$

$$v_{s,i}(0) = v_{s,i}(a) + \frac{6F_i a}{5G_i b h_i} \tag{64}$$

whose calculations benefit from the negligible terms on $e^{\lambda(a-L)}$ and lead at last to $v_i(0) = v_{b,i}(0) + v_{s,i}(0)$.

3. Materials and methods

As mentioned in Section 1, the scope of this paper are adhesive joints between dissimilar steel and aluminium adherends. The Young's moduli here adopted were 200 GPa for steel and 70 GPa for aluminium, while the Poisson's ratio was 0.3. E_a = 2 GPa and v_a = 0.35 typical of structural adhesives were assumed. The bondline thicknesses (Fig. 1) considered were the thin h_a = 0.2 mm and the moderately thick h_a = 1.0 mm.

As for specimen geometry, the high toughness of many structural adhesives and the need to avoid premature adherend yielding are known to demand relatively thick metal adherends [3,12,16]. One of the goals of this work was to evaluate the DABM for different adherend thicknesses. Therefore, h_i = 5-20 mm were employed, leading to h_2/h_1 = 1-4. In addition, the approximations in the treatment of transverse shear discussed in Section 2.1 warranted DABM evaluation for relatively small a/h_2 ratios, which increase the contribution of transverse shear to specimen behaviour. Accordingly, low a/h_2 = 6 to high a/h_2 = 12 were

used in order to assess the effects of errors brought about by the aforementioned transverse shear modelling approximations. Given the adherend thicknesses adopted, this resulted in crack lengths a = 60-160 mm and in a/h_1 = 6-32.

Finally, the simplified solutions proposed in Section 2.3 rest on the hypothesis that the crack-tip is sufficiently distant from the built-in end (Fig. 1). Having selected the adherend materials, h_1, h_2 and a, the criterion discussed in Section 2.3 demands choosing a minimum L so that

$$\tau_0 + \tau_1 e^{-\lambda L} \approx 1.001\tau_0 \;\Leftrightarrow\; L \approx \frac{1}{\lambda}\ln\left(\frac{10^3\cdot\tau_1}{\tau_0}\right) \tag{65}$$

However, in order to facilitate the comparison and interpretation of results, L was determined approximately for the critical case, and its value was kept for specimens with identical h_1, h_2 and h_a. As expected from previous work on mode II fracture of ENF specimens [12,16], the critical case was the one of steel adherends, which promote lower λ. For the same reason, thicker bondlines also require longer specimens. Table 1 summarizes the set of specimen geometries analysed in this paper.

Table 1. Specimen geometries adopted.

h_1 (mm)	h_2 (mm)	a (mm)	h_a (mm)	L (mm)
10	10	60-100	0.2	200
			1.0	270
5	10	60-100	0.2	200
			1.0	270
5	20	120-160	0.2	270
			1.0	370

The DABM predictions were compared to FEA performed with the Abaqus® code. The two-dimensional (2D) models were constructed with 8-node solid quadratic reduced integration elements. Owing to the beam-like geometry, plane stress was assumed for the

adherends. The bondline was in turn modelled with plane strain elements, given the strong constraints imposed by the stiff adherends. These modelling conditions find support in previous studies on mode I and mode II fracture of adhesively bonded metals [11,12,16]. Preliminary mesh refinement studies showed that each adherend could be modelled by 4 (h_1 = 5 mm) to 8 (h_2 = 20 mm) layers of elements, while 2 (h_a = 0.2 mm) or 4 (h_a = 1.0 mm) layers of elements were appropriate for the bondline. The maximum element length was 1 mm, but in the crack-tip vicinity the length was reduced to 0.1 mm so that accurate G_I and G_{II} could be computed by the virtual crack closure technique (VCCT).

Regarding the results presented below, the F_1 and F_2 loads (Fig. 1) imposed to both DABM and FEA never brought about geometric non-linearity. Moreover, the load combinations aimed at achieving $G_{II}/G \approx 5$, 20, 50, 80 and 95 %, as obtained from the DABM, G being the total strain-energy release rate ($G_I + G_{II}$). No attempt was made to obtain the F_2/F_1 ratios leading to pure modes I and II. For the sake of conciseness, the load-point displacements sum

$$\Delta = |v_1(0)| + |v_2(0)| \tag{66}$$

was used for comparing DABM and FEA results. Finally, in order to show the relevance of crack-tip flexibility, which gives rise to the well-known crack length corrections of corrected beam theory [17], DABM predictions for G were compared to those of BT prediction [18]

$$G_{BT} = \frac{1}{2b}\left\{\frac{M_1^2(a)}{E_1 I_1} + \frac{M_2^2(a)}{E_2 I_2} - \frac{[M_1(a)+M_2(a)]^2}{\Theta}\right\} \tag{67}$$

where M_i are given by Eqs. (48),

$$\Theta = \frac{b}{3}\{E_2(y_2^3 + h_n^3) + E_1[(y_2 + h_a + h_1)^3 - (y_2 + h_a)^3]\} \tag{68}$$

is the bending stiffness of the uncracked region (Fig. 1) and h_n and y_2 are computed from Eqs. (33) and (34), respectively.

4. Results and discussion

The following remarks are needed on the results presented below:

- Mode-mix results for the larger a = 100 and 160 mm crack lengths (Table 1) are not presented, because they are quasi-identical to the ones obtained for a = 60 and 120 mm, respectively. This shows that G_{I} and G_{II} are, to a very large extent, dictated by the crack-tip bending moments $M_{\mathrm{i}}(a)$;
- Accordingly, transverse shear plays a minor role, despite the relatively small a/h_2 considered. This means that the approximations inherent to the treatment of transverse shear discussed in Section 2.1 end-up having a marginal effect;
- For the sake of clarity and conciseness, results for the thicker h_a = 1.0 mm bondline are only depicted when they differ significantly from h_a = 0.2 mm cases.

Figs. 3 and 4 present the G_{II}/G mode-mix ratios for various combinations of adherend materials, bondline thicknesses and specimen geometries (see Fig. 1 and Table 1). It can be seen that:

- even when adherends are made of identical metals, their elastic properties have a non-negligible effect on the mode-mix via the λ, μ and ω traction distribution parameters;
- the h_a-effect on G_{II}/G tends to be more pronounced for high mode I loadings and for larger adherend flexural stiffness mismatch i.e. higher E_2I_2/E_1I_1 ratio; this can be explained by the larger crack-tip section relative displacements in mode I dominated set-ups;
- the interval of F_2/F_1 ratios needed to achieve the $G_{\mathrm{II}}/G \approx$ 5-95 % range becomes wider for higher E_2I_2/E_1I_1; again, this reflects the dominance of bending moments on the behaviour of beam-like specimens;
- there is clearly very good agreement between DABM and FEA results.

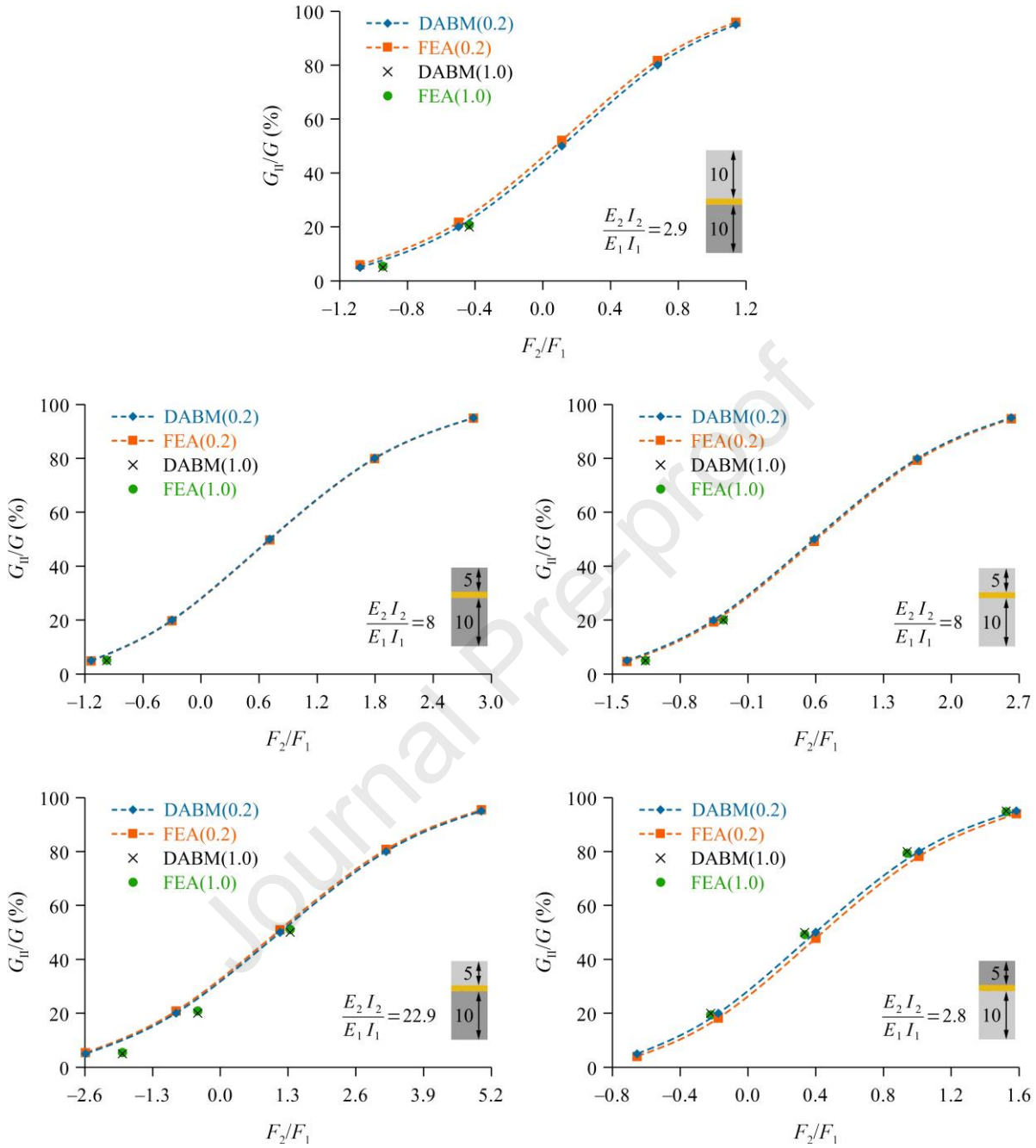

Fig. 3. Mode II ratio in FLDCB specimens (Fig. 1, Table 1) with a = 60 mm, h_a = 0.2 and 1.0 mm. Sketches embedded in the plots depict the adherend materials (aluminium in light grey, steel in dark grey) and thicknesses.

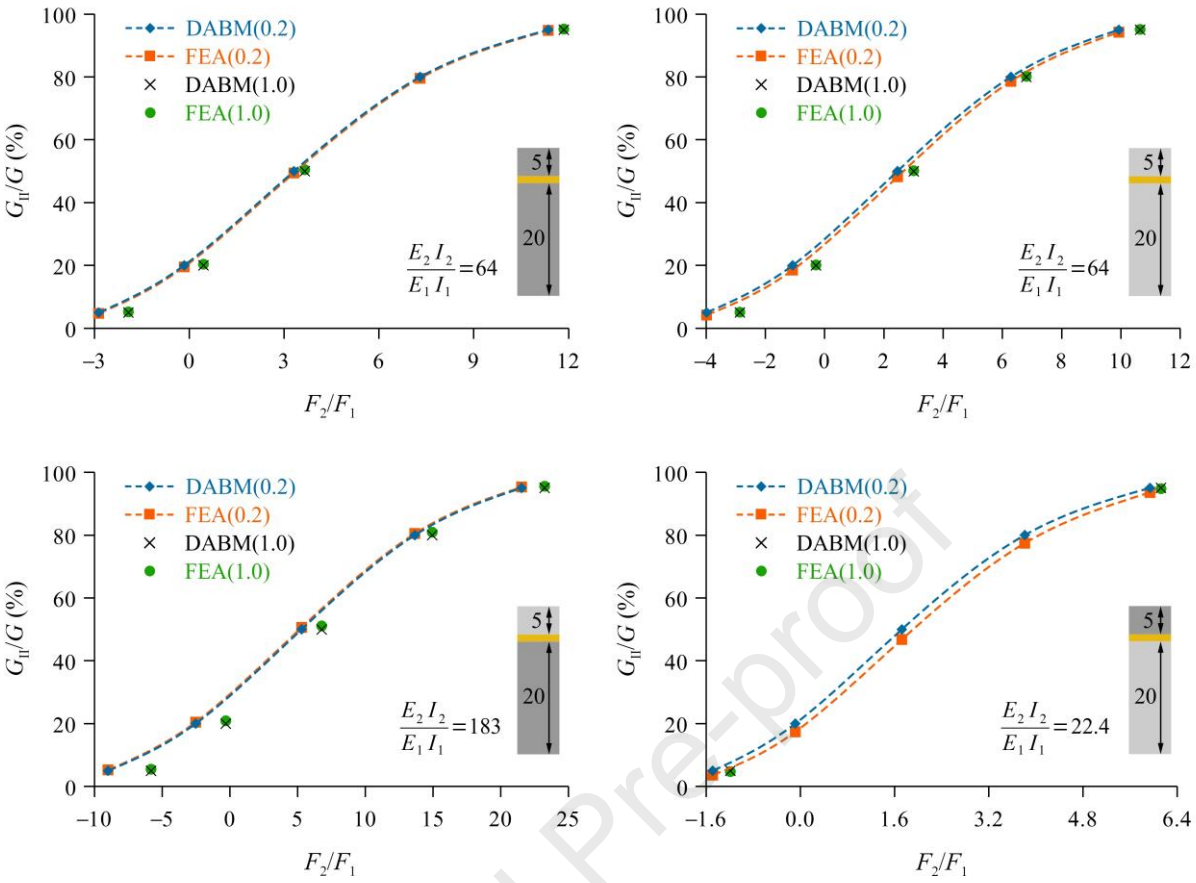

Fig. 4. Mode II ratio in FLDCB specimens (Fig. 1, Table 1) with a = 120 mm, h_a = 0.2 and 1.0 mm. Sketches embedded in the plots depict the adherend materials (aluminium in light grey, steel in dark grey) and thicknesses.

As seen in a recent review [7], mode-mix predictions have been a major challenge in adhesive joints with dissimilar adherends. The present results show that the DABM is very accurate when metal adherends are involved.

The very good performance of the DABM is confirmed by the accurate predictions for normalized G (Fig. 5) and load-point displacements sum Δ (Fig. 6). The errors defined as differences relative to FEA results are usually larger for the thicker h_a = 1.0 mm bondline, but always under 2%. Therefore, the DABM provides a complete analysis framework for the fracture of dissimilar metal joints. Its ability to model quite accurately crack-tip flexibility effects is of particular importance for adhesive joints. This is clearly demonstrated in Fig. 7, which shows that DABM G predictions can be much higher than BT Eq. (67), especially for

thicker bondlines and mode II dominated setups.

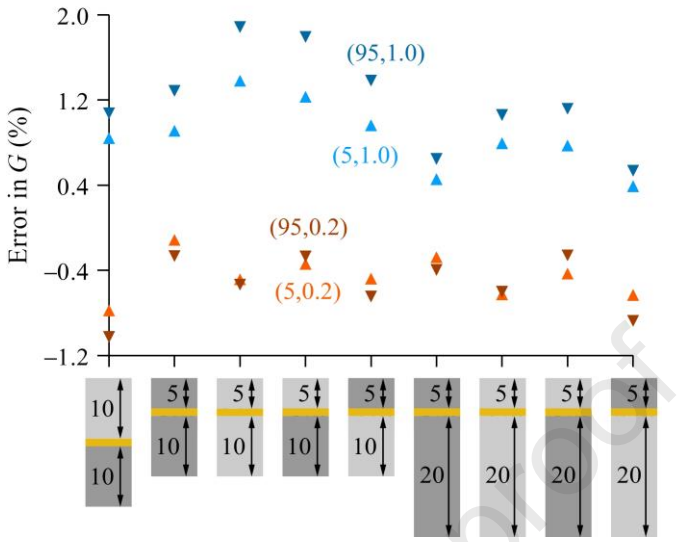

Fig. 5. Errors in G predictions of DABM for various specimens analysed (see text, Fig. 1 and Table 1) with the (G_{II}/G, h_a) combinations marked. Sketches represent aluminium and steel adherends in light and dark grey, respectively.

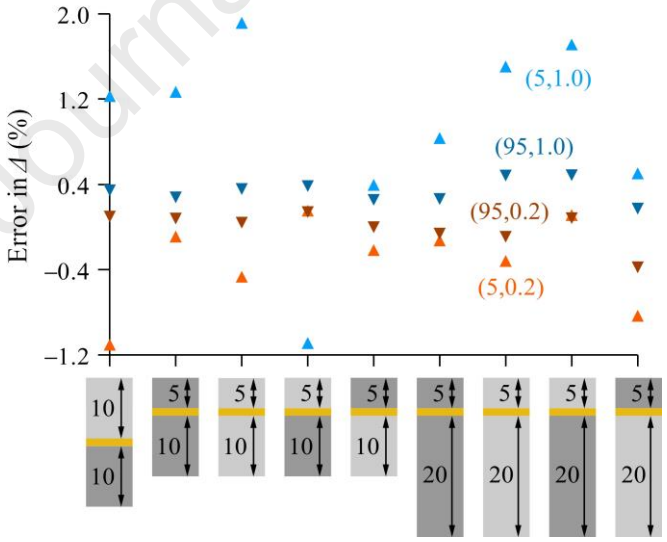

Fig. 6. Errors in the load-point displacements sum Δ predictions of DABM for various specimens analysed (see text, Fig. 1 and Table 1) with the (G_{II}/G, h_a) combinations marked. Sketches represent aluminium and steel adherends in light and dark grey, respectively.

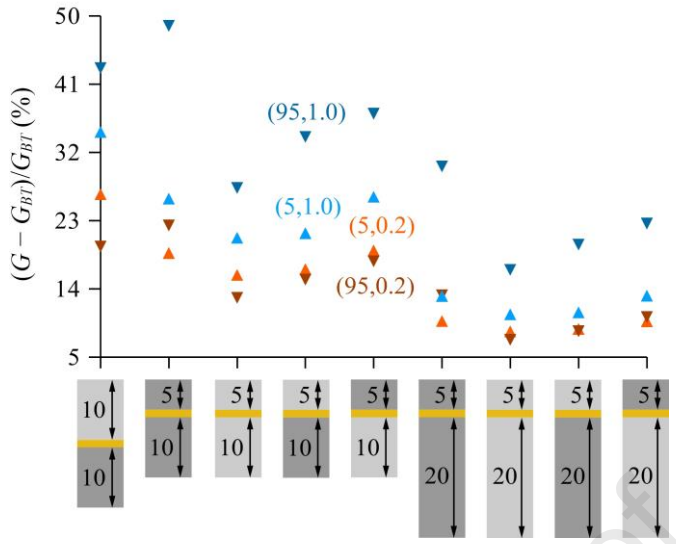

Fig. 7. G predictions of DABM relative to beam theory (BT) for various specimens analysed (see text, Fig. 1 and Table 1) with the (G_{II}/G, h_a) combinations marked. Sketches represent aluminium and steel adherends in light and dark grey, respectively.

In actual fracture tests, one may always apply the compliance calibration method to derive the total strain-energy release rate G. Nevertheless, BT based approaches such as the DABM provide useful benchmarks for experimental compliance values. Moreover, in the case of specimens with identical adherends, beam models yield accurate mode I and mode II fracture toughness values when using the effective crack concept [3,11,12,16]. As discussed above, the DABM also lends itself to this approach, but its real adequacy requires future investigation.

5. Interest and potential of dissimilar metal adherend fracture specimens

The above results show that the DABM provides a suitable framework for analysing the fracture of dissimilar metal adhesive joints. The availability of accurate and easy-to-apply data reduction schemes is indeed an important requirement for fracture specimens. However, the interest in testing dissimilar metal adhesive joints can be questioned considering that:

- in adequately prepared joints, fracture should be cohesive within the adhesive layer

and thus, in principle, give rise to toughness values that are adherend-independent; one condition for this argument to hold is that adherends are always stiff enough to constrain the bondline into the uni-axial strain state here assumed;

- the entire range of mixed-mode I-II combinations can nowadays be achieved with fracture tests on specimens with identical metal adherends [3].

In fact, fracture toughness values measured with dissimilar adherend specimens may be more affected by residual stresses that develop upon cooling from adhesive cure temperature. This is due to the mismatch of adherend elastic properties, thicknesses and thermal of expansion coefficients. Tsokanas et al. [19] modelled the effects of residual stresses on G and on mode partitioning in terms of additional crack-tip section forces and moments. They [19] concluded that residual stresses may have a significant effect on moment-loaded double cantilever beam specimens with titanium and composite adherends. Although some of the effects of residual stresses can be accounted for through beam modelling, the role of bondline axial σ_x stresses cannot. The same applies to CZM with FEA, since only out-of-plane stresses and the corresponding I-II-III fracture modes are taken into account. Moreover, other well-known difficulties in determining residual stresses in polymers and polymer matrix composites are also relevant i.e. temperature-dependent properties and visco-elasticity at high temperatures. Therefore, one of the motivations for testing dissimilar adherend joints is precisely to assess the effects of residual stresses by taking as reference toughness values measured with identical adherend specimens.

Regarding the determination of the whole mixed-mode I-II fracture envelope, the tests that allow several mode-mix combinations on specimens with identical adherends demand elaborate fixtures [3-6]. Moreover, long specimens are needed to accommodate the large FPZ that tough adhesives develop, especially under mode II dominated loadings. In fact, it has been shown that FPZ getting near support and load points can lead to artificially high

perceived mode II fracture toughness values [12,16]. Therefore, another possible advantage of dissimilar adherend specimens could be to provide a considerable range of mixed-mode I-II combinations with simple test fixtures. The simplest mixed-mode tests currently available are [3] the ADCB, the fixed-ratio mixed mode (FRMM) and the single-leg bending (SLB). Actually, both the ADCB and FRMM tests can be seen as particular cases of the FLDCB (Fig. 1) here adopted: $F_2 = -F_1$ in the former and there is no need for the built-in end, while $F_2 = 0$ for the latter test. Evidently, in practice, the SLB specimen will be longer, but, on the other hand, uncertainties in clamp rigidity are avoided. Anyway, the DABM showed that G and the mode-mix are dictated by the $M_i(a)$ crack-tip section bending moments. Therefore, where these two major test characteristics are concerned, the SLB and FRMM are on identical grounds.

Accordingly, the following analysis aimed at evaluating the potential of those simple tests for:

- covering a wide range of mixed-mode combinations;
- allowing the measurement of high G_c values typical of tough adhesives without metal adherend yielding.

The maximum crack-tip section adherend bending stress

$$\sigma_{b,i} = \frac{6F_i a}{b h_i^2} \tag{69}$$

was limited to 1300 MPa for steel adherends, a value well within the reach of high strength steels, and to 400 MPa for aluminium adherends, which does imply selecting more specific high-strength grades. Table 2 presents several FRMM or SLB specimen adherends and geometries that are quite interesting, as they cover a wide G_{II}/G = 16-78 % range and allow measurements on adhesives with quite high G_c. Two crack lengths differing by 40 mm were considered to show that the mode-mix remains nearly constant throughout such a significant crack propagation length.

Table 2. FRMM specimen (consider $F_2 = 0$ in Fig. 1) adherends and dimensions deemed of interest for characterising the mixed-mode I-II fracture envelope. G_{max} corresponds to reaching the maximum $\sigma_{b,i}$ = 1300 MPa for steel adherends and 400 MPa for aluminium adherends.

E_1 (GPa)	h_1 (mm)	E_2 (GPa)	h_2 (mm)	a (mm)	h_a (mm)	G_{max} (kJ/m^2)	G_{II}/G (%)
200	5	70	20	120 – 160	0.2	7.5 – 7.4	21.2 – 21.3
					1.0	7.8 – 7.6	18.5 – 18.4
70	15	200	15	90 – 130	0.2	6.3 – 5.9	44.6 – 45.3
					1.0	6.9 – 6.4	42.1 – 42.0
70	20	200	5	120 – 160	0.2	5.9 – 5.7	70.5 – 70.6
					1.0	6.9 – 6.5	75.9 – 75.8
200	5	200	20	120 – 160	0.2	7.6 – 7.4	21.2 – 21.4
					1.0	7.8 – 7.6	16.4 – 16.4
200	15	200	13	90 – 130	0.2	22.6 – 21.1	45.3 – 45.5
					1.0	26.5 – 23.8	50.8 – 50.1
200	20	200	5	120 – 160	0.2	16.8 – 16.1	70.1 – 70.2
					1.0	21.2 – 19.5	77.8 – 77.6

In addition to the above specimens, it is also worth considering the quasi-pure mode I condition (G_{II}/G = 0.6-0.7%) that can be attained with an ADCB test on steel/aluminium specimens having (Fig. 1) h_1 = 5 mm, h_2 = 10 mm, a = 60-100 mm. Such specimens allow the measurement of high G_c = 10.6 and G_c = 11.0 kJ/m^2 for h_a = 0.2 mm and h_a = 1.0 mm, respectively, for the aforementioned limit $\sigma_{b,i}$. Evidently, in practice, other issues need to be considered when selecting the specimen geometry i.e. accommodate a large FPZ and the possibility of large displacements. Nonetheless, the high potential of dissimilar metal adherend specimens is quite clear.

6. Conclusions

A beam model was here developed for mixed-mode I-II fracture testing adhesive joints with dissimilar metal adherends. The model proved to predict quite accurately the strain-energy release rate, mode-mix and load-point displacements of several specimens with:

- aluminium/aluminium, steel/steel and aluminium/steel adherends;
- thicker-to-thin adherend thickness ratios from 1 to 4;
- bondline thicknesses from 0.2 to 1.0 mm;
- loadings generating mode II ratios from 5 to 95 %.

The results obtained show that the strain-energy release rate and mode-mix are clearly dominated by the crack-tip section bending moments. This ensures that the approximations involved in dealing with transverse shear do not affect significantly the accuracy of model predictions.

In spite of somewhat lengthy developments and expressions, the present model is entirely closed-form i.e. it does not require any numerical iterative calculations. Furthermore, calculations could be further alleviated by:

- grasping the physical meaning of the traction solution parameters;
- selecting specimens whose uncracked part is long enough to avoid interaction between crack-tip and support (or load-point) local traction fields.

This greatly facilitates planning of experiments, including specimen adherend materials and geometry selection, as well as subsequent experimental data reduction.

Finally, a preliminary study showed the enormous potential of dissimilar metal bonded specimens for attaining a wide range of mode-mix combinations with well-known simple tests. Dissimilar metal bonded specimens could therefore be an interesting alternative to the mixed-mode tests on common specimens with identical adherends that demand elaborate fixtures.

Acknowledgments

This work was supported by the Foundation for Science and Technology (FCT) - Aveiro Research Centre for Risks and Sustainability in Construction (RISCO), Universidade de Aveiro, Portugal [FCT/UIDB/ECI/04450/2020].

References

[1] Meschut G, Janzen V, Olfermann T. Innovative and highly productive joining technologies for multi-material lightweight car body structures. J Mater Eng Perform 2014; 23: 1515-23. https://doi.org/10.1007/s11665-014-0962-3.

[2] Ramalho LDC, Campilho RDSG, Belinha J, da Silva LFM. Static strength prediction of adhesive joints: A review. Int J Adhes Adhes 2020; 96: 102451. https://doi.org/10.1016/j.ijadhadh.2019.102451.

[3] Chaves FJP, da Silva LFM, de Moura MFSF, Dillard DA, Esteves VHC. Fracture mechanics tests in adhesively bonded joints: A literature review. J Adhes 2014; 90: 955-92. https://doi.org/10.1080/00218464.2013.859075.

[4] Fernlund G, Spelt JK. Mixed-mode fracture characterization of adhesive joints. Compos Sci Technol 1994; 50: 441-9. https://doi.org/10.1016/0266-3538(94)90052-3.

[5] Singh HK, Chakraborty A, Frazier CE, Dillard DA. Mixed mode fracture testing of adhesively bonded wood specimens using a dual actuator load frame. Holzforschung 2010; 64: 353-61. https://doi.org/10.1515/hf.2010.041.

[6] Costa M, Carbas R, Marques E, Viana G, da Silva LFM. An apparatus for mixed-mode fracture characterization of adhesive joints. Theor Appl Fract Mech 2017; 91: 94-102. https://doi.org/10.1016/j.tafmec.2017.04.014.

[7] Wang W, de Freitas ST, Poulis JA, Zarouchas D. A review of experimental and theoretical fracture characterization of bi-material bonded joints. Compos Part B 2021; 206: 108537. https://doi.org/10.1016/j.compositesb.2020.108537.

[8] Bennati S, Colleluori M, Corigliano D, Valvo PS. An enhanced beam-theory model of the asymmetric double cantilever beam (ADCB) test for composite laminates. Compos Sci Technol 2009; 69: 1735-45.

https://doi.org/10.1016/j.compscitech.2009.01.019.

[9] Bennati S, Fisicaro P, Taglialegne L, Valvo PS. An elastic interface model for the delamination of bending-extension coupled laminates. Appl Sci 2019; 9: 3560. https://doi.org/10.3390/app9173560.

[10] de Morais AB. Interlaminar fracture of asymmetrically delaminated specimens: beam modelling and noteworthy characteristics. Compos Struct 2021; 265: 113745. https://doi.org/10.1016/j.compstruct.2021.113745.

[11] de Morais AB. Analysis of the metal adhesively bonded double cantilever beam specimen. Int J Adhes Adhes 2015; 61: 8-14. http://dx.doi.org/10.1016/j.ijadhadh.2017.01.003.

[12] de Morais AB. Elastic-plastic analysis of the adhesively bonded end-notched flexure specimen. Eng Fract Mech 2018; 188: 80-92. http://dx.doi.org/10.1016/j.engfracmech.2017.07.021.

[13] Weißgraeber P, Stein N, Becker W, 2014. A general sandwich-type model for adhesive joints with composite adherends. Int J Adhes Adhes 2014; 55:56-63. http://dx.doi.org/10.1016/j.ijadhadh.2014.06.009.

[14] Liu X, Huang Y, Yin Z, Bennati S, Valvo PS. A general solution for the two-dimensional stress analysis of balanced and unbalanced adhesively bonded joints. Int J Adhes Adhes 2014;54:112-123. http://dx.doi.org/10.1016/j.ijadhadh.2014.05.011.

[15] Alfredsson KS, Högberg JL. A closed-form solution to statically indeterminate adhesive joint problems—exemplified on ELS-specimens. Int J Adhes Adhes 2008; 28: 350-361. http://dx.doi.org/10.1016/j.ijadhadh.2007.10.002.

[16] de Morais AB. Determination of the shear traction-separation law of adhesive layers using the end-notched flexure specimen. Eng Fract Mech 2020; 253: 107199. https://doi.org/10.1016/j.engfracmech.2020.107199.

[17] Wang Y, Williams JG. Corrections for Mode II fracture toughness specimens of composites materials. Compos Sci Technol 1992; 43: 251-6. https://doi.org/10.1016/0266-3538(92)90096-L.

[18] Williams JG. On the calculation of energy release rates for cracked laminates. Int J Fract 1988; 36: 101-19. https://doi.org/10.1007/BF00017790.

[19] Tsokanas P, Loutas T, Kotsinis G, van den Brink WM, Nijhuis P. Strain energy release rate and mode partitioning of moment-loaded elastically coupled laminated beams with hygrothermal stresses. Compos Struct 2021; 259: 113237. https://doi.org/10.1016/j.compstruct.2020.113237.

[20] Irving RS. Integers, polynomials, and rings: a course in algebra. New York: Springer-Verlag; 2004.

Appendix

As seen in Section 2.2, the solution of Eq. (23) demands finding the roots of the 3rd-order polynomial equation

$$\frac{h_a}{G_a}t^3 + D_5 t^2 + D_3 t + D_1 = 0 \tag{A1}$$

where $t = s^2$ defined in Eq. (27) and the D_1-D_5 coefficients are given by Eqs. (24)-(26). The procedures for finding the roots of Eq. (A1) can be found in [20]. First, the discriminant

$$\Delta_d = 18\frac{G_a}{h_a}D_5 D_3 D_1 - 4D_5^3 D_1 + D_5^2 D_3^2 - 4\frac{G_a}{h_a}D_3^3 - 27\frac{G_a^2}{h_a^2}D_1^2 \tag{A2}$$

dictates the types of roots. For the combinations of metal adherends, adhesive properties and thicknesses here considered, $\Delta_d < 0$ and thus Eq. (A1) has one real root and two complex conjugate roots. This means that the 6th-order polynomial has two real symmetric roots and two pairs of complex conjugate roots, here designated as $\pm\lambda$ and $\pm(\mu \pm i\omega)$, where $i^2 = -1$. The roots can be obtained from

$$\lambda = \sqrt{\frac{-G_a}{3h_a}\left(D_5 + R + \frac{\Delta_0}{R}\right)} \tag{A3}$$

$$\mu = \sqrt{\frac{G_a}{12h_a}\left(\sqrt{S^2 + 3\left(\frac{\Delta_0}{R} - R\right)^2} + S\right)} \tag{A4}$$

$$\omega = \sqrt{\frac{G_a}{12h_a}\left(\sqrt{S^2 + 3\left(\frac{\Delta_0}{R} - R\right)^2} - S\right)} \tag{A5}$$

where

$$S = \frac{\Delta_0}{R} + R - 2D_5 \tag{A6}$$

$$R = \sqrt[3]{\frac{\Delta_1 + \sqrt{\Delta_1^2 - 4\Delta_0^3}}{2}} \tag{A7}$$

$$\Delta_0 = D_5^2 - 3\frac{h_a}{G_a}D_3 \tag{A8}$$

$$\Delta_1 = 2D_5^3 - 9\frac{h_a}{G_a}D_5 D_3 + 27\frac{h_a^2}{G_a^2}D_1 \tag{A9}$$

ELSEVIER SCIENCE

MANUSCRIPT ACCEPTANCE FORM

(to be filled in by the corresponding author and returned to the editor with the finally accepted electronic version of the manuscript)

Name of Journal: *INTERNATIONAL JOURNAL OF ADHESION AND ADHESIVES*

Ref: J1969

Title: A beam model for the fracture of adhesive joints with dissimilar metal adherends
by Alfredo B. de Morais

Corresponding author's name: Alfredo B. de Morais

Please ensure that the following information is supplied for the corresponding author:

☒ E-mail address abm@ua.pt

☒ Full postal address University of Aveiro, Department of Mechanical Engineering, Campus Santiago, 3810-193 Aveiro, Portugal

☒ Telephone and fax numberTel.: +351 234 370830; fax: +351 234 370953

Checklist:

☒ Are the keywords supplied?
☒ Are all figures supplied with captions?
☒ Are all tables supplied, and with captions?
☒ Are copyright permission letters enclosed for any artwork/tables previously published, including those published on the world-wide-web?

No copyright permission letters needed.

If any of the illustrations are to be printed in colour please indicate this below: note that in the printed paper, colour costs you about 300 Euros per Fig, while on-line, colour is free

I do not wish that illustrations are printed in colour. Colours should be kept only in the online version.